



Contents lists available at ScienceDirect

## International Journal of Solids and Structures

journal homepage: [www.elsevier.com/locate/ijsoistr](http://www.elsevier.com/locate/ijsoistr)

## Effects of coating on dynamic stress concentration in fiber reinforced composites

Xiangjun Peng<sup>a,b</sup>, Wei He<sup>b</sup>, Fengxian Xin<sup>b</sup>, Guy M. Genin<sup>a,d,\*</sup>, Tian Jian Lu<sup>c,e,\*</sup><sup>a</sup>U.S. National Science Foundation Science and Technology Center for Engineering Mechanobiology, and Department of Biomedical Engineering, Washington University, St. Louis, MO 63130, USA<sup>b</sup>State Key Laboratory for Strength and Vibration of Mechanical Structures, Xi'an Jiaotong University, Xi'an 710049, PR China<sup>c</sup>State Key Laboratory of Mechanics and Control of Mechanical Structures, Nanjing University of Aeronautics and Astronautics, Nanjing 210016, PR China<sup>d</sup>Bioinspired Engineering and Biomechanics Center (BEBC), Xi'an Jiaotong University, Xi'an 710049, PR China<sup>e</sup>Nanjing Center for Multifunctional Lightweight Materials and Structures (MLMS), Nanjing University of Aeronautics and Astronautics, Nanjing 210016, PR China

## ARTICLE INFO

## Article history:

Received 27 October 2020  
 Received in revised form 21 February 2021  
 Accepted 10 March 2021  
 Available online 16 March 2021

## Keywords:

Fiber reinforced composite  
 Dynamic stress concentration  
 Coating

## ABSTRACT

Fiber reinforced materials consisting of aligned fibers within a matrix are effective for applications in nature and engineering in which strength and stiffness are required in a dominant direction. The fibers are typically coated. Optimization of these materials is typically based upon choosing elastic properties of phases to reduce static stresses. However, materials with well-matched moduli can have mismatched acoustic impedance, and thus a fiber reinforced material that is strong in quasistatic loading may be weak in dynamic loading. To explore this trade-off, we modeled perfectly bonded, isotropic, linear elastic coated fibers in an infinite, isotropic, linear elastic matrix and calculated dynamic stresses and interfacial stress concentrations induced by continuous and transient waves using the wave function expansion method. Results revealed ways that the physical properties and geometrical dimensions of a coating around a fiber can be tailored to reduce dynamic stress concentration, and point to a pathway for improving the shock resistance of fiber reinforced materials.

© 2021 Elsevier Ltd. All rights reserved.

## 1. Introduction

The ever-increasing demand for materials with high strength and stiffness and low mass continues to promote the development of advanced fiber reinforced composite materials (Ashby and Cebon, 1993). However, the fibrous components that endow composites with high strength and stiffness to weight ratios also introduce new failure mechanisms that must be understood to improve failure and fatigue properties and make use of composites at their fullest potential, especially for high-risk applications such as aircraft structures (Kyriakides et al., 1995; Lu, 1996; Evans et al., 1995; Genin and Hutchinson, 1999, 1997). Numerous; theoretical, and experimental approaches to understand these mechanisms have uncovered a central role for matrix microcracks that can on the one hand energy absorption and stress redistribution (Genin and Hutchinson, 1999, 1997; Aveston and Kelly, 1973; Budiansky et al., 1986; Rajan and Zok, 2013), but can on the other hand coalesce to form deleterious macrocracks (Paskaramoorthy and Meguid, 1999; Davidson, 1991). Under dynamic loading, dynamic

stress concentrations arising from mismatches between the elastic and thermal properties of the fiber and matrix may promote microcracking, and are therefore a focus of research (Bugarin et al., 2012).

Analysis of the internal stress fields in fiber (Kyriakides et al., 1995) and particle (Wang et al., 1993; Kassam et al., 1995) reinforced composites builds from the Eshelby solution (Eshelby, 1957); which predicts uniform strain fields within an ellipsoidal inclusion bonded to a uniformly strained infinite medium (Benveniste et al., 1989), and has been extended to include the effects of coatings on the reinforcement (Bonfoh et al., 2012; Chen et al., 2019a, 2019b; Lipinski et al., 2006; Sarvestani, 2003; Achenbach and Zhu, 1989). In engineering, these coatings emerge during processing due to chemical reactions between the reinforcement and the surrounding matrix, especially in high temperature composites, and may also be created deliberately by coating the fibers (Gillies and Lieber, 2011). In biology, many fibers develop coatings, such as the myelin coatings on axons, the endomysium surrounding muscle fibers, perimysium surrounding fibrous muscle fascicles, the epimysium surrounding muscles, and epitenon and endotenon in tendons (Mouw et al., 2014; Podratz et al., 2001; Choi et al., 2007). Similarly, many cells are surrounded by

\* Corresponding author.

E-mail addresses: [genin@wustl.edu](mailto:genin@wustl.edu) (G.M. Genin), [tjlu@nuaa.edu.cn](mailto:tjlu@nuaa.edu.cn) (T.J. Lu).

coatings, notably chondrocytes in cartilage (Saadat, 2018; Madhukar and Drzal, 1991).

In the case of static loads, these coatings are well-studied and are known to affect the strength, stiffness, and internal stress fields of the composite or tissue (Gillies and Lieber, 2011; Walpole, 1978). Walpole (cf. Mikata and Taya, 1985) showed that a thin coating on an inclusion has a pronounced effect on stress and strain fields in the matrix, and Mikata and Taya (Chen et al., 2018) showed similar effects in thermo-mechanical loading. Coatings around cells can modulate the membrane stress and kinematic fields to affect fluid transport and surface interactions (Chen et al., 2019; Madhukar and Drzal, 1991; Ghosn and Lerch, 1989). These effects have been exploited in engineered composites, including efforts to reduce microcracking by minimizing residual stresses in the matrix (Evans et al., 1991), to increase and control microcracking for the purpose of protecting fibers and enhancing composite toughness (Aveston and Kelly, 1973; Budiansky et al., 1986; Zhang et al., 2018); or to enhance strength and stiffness (Carman et al., 1993; Frueh et al., 2018). In the case of ceramic matrix composites, weak coatings are critical to toughness, so much so that they must be designed to resist strengthening through oxidation (Bogan and Hinders, 1993). However, these enhancements have been made for improving responses to quasistatic loadings only, in which inertial effects can be neglected.

Under sufficient dynamic loading, the role of inertia is no longer negligible. Typically, the energy of a dynamic load is transmitted in the form of waves travelling through the matrix of the composite (Bugarin et al., 2012; Wang et al., 2007). Upon meeting obstacles such as fibers, these waves are scattered, leading to complicated stress patterns and higher local stresses (stress concentrations). Dynamic stresses may induce microcracking and nucleate failure at interfaces between the matrix, coating, and fibers. The mechanics of dynamic stress concentrations associated with coatings needs to be further explored for designing composite materials with enhanced mechanical properties.

The theoretical approach of this paper is complementary to a large body of advanced numerical treatments of acoustics in solids. These numerical treatments, mostly using finite element and finite difference approaches, are now robust, convenient, and well-validated (Pamel, 2017; Xu and Yu, 2017; Pao et al., 1973). However, these numerical methods require closed form solutions for validation, and offer only approximations to analytical solutions. For the problem studied in this paper, the theoretical solution offers two types of insight that numerical solutions cannot. First, it provides scaling laws for the effects of coatings on fibrous reinforced composite subjected to continuous elastic waves and transient waves. Second, it allowed for clear delineation of the effects of quasistatic and dynamic stress. We believe that this insight will

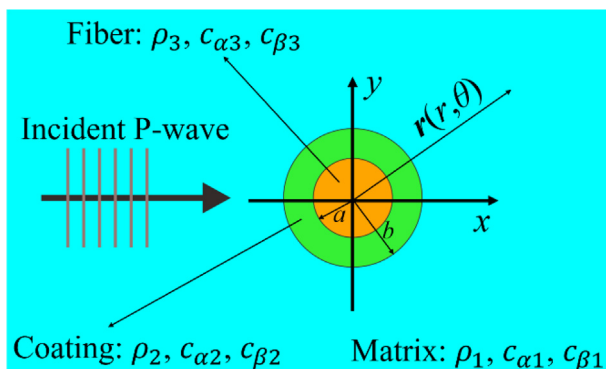


Fig. 1. Schematic of wave scattering by a coated cylindrical fiber embedded in an infinite matrix.

be of value for structural and material optimization of these material systems.

## 2. Theoretical model

Consider an infinite, linearly elastic medium containing an infinitely long, coated, cylindrical, linear elastic fiber of radius  $a$  aligned with the  $z$  axis of a cylindrical  $(r, \theta, z)$  coordinate system (Fig. 1). The matrix (phase  $i = 1$ ), coating (phase  $i = 2$ ) and fiber (phase  $i = 3$ ) are perfectly bonded, and are linear, elastic and isotropic. Dynamic excitation is provided by an incident plane compressional wave traveling in an arbitrarily chosen  $x$  direction in an  $x$ - $y$  plane perpendicular to the  $z$  axis. Plane strain conditions prevail so that the linearized strain components  $\varepsilon_{zz} = \varepsilon_{xz} = \varepsilon_{yz} = 0$ , and field quantities such as the displacements, strains, and stresses are independent of  $z$ .

### 2.1. Governing equations

In the absence of body forces, the equation of motion for displacement vector  $\mathbf{u}$  is (Pao and Mow, 1976; Pao, 1962)

$$(\lambda_i + 2\mu_i)\nabla\nabla\mathbf{u} + \mu_i\nabla^2\mathbf{u} = \rho_i\ddot{\mathbf{u}} \quad (1)$$

where  $\lambda_i$  and  $\mu_i$  are the Lamé elastic constants of material phase  $i$ ,  $\nabla$  is the gradient operator, and  $\rho_i$  is the density of material phase  $i$ .

The displacement  $\mathbf{u}$  may be expressed advantageously as the superposition of the gradient of a scalar potential and the curl of a vector potential, as (Pao and Mow, 1976; Pao, 1962)

$$\mathbf{u} = \nabla\varphi + \nabla \times \boldsymbol{\psi} \quad (2)$$

where  $\varphi$  is the plane compressional wave potential and  $\boldsymbol{\psi}$  is the transversely polarized shear wave potential. Inserting (2) into (1) leads to two scalar wave equations (Pao and Mow, 1976):

$$\nabla^2\varphi = \frac{1}{c_{zi}^2}\varphi \quad (3)$$

$$\nabla^2\boldsymbol{\psi} = \frac{1}{c_{\beta i}^2}\boldsymbol{\psi} \quad (4)$$

where  $c_{zi} = \sqrt{(\lambda_i + 2\mu_i)/\rho_i}$  is compressional wave velocity in material  $i$  and  $c_{\beta i} = \sqrt{\mu_i/\rho_i}$  is the shear wave velocity in material  $i$ . In the current plane-strain problem, there is no displacement in the  $z$ -direction. Thus,  $\boldsymbol{\psi}$  has no component in the  $r$ - or the  $\theta$ -direction and reduces to  $\boldsymbol{\psi} = \psi\mathbf{e}_z$ ,  $\mathbf{e}_z$  being the unit vector in the  $z$ -direction. Consequently, in cylindrical coordinates, the displacement components can be expressed in terms of  $\varphi$  and  $\psi$  by (Pao and Mow, 1976)

$$\begin{aligned} u_r &= \frac{\partial\varphi}{\partial r} + \frac{1}{r}\frac{\partial\psi}{\partial\theta} \\ u_\theta &= \frac{1}{r}\frac{\partial\varphi}{\partial\theta} - \frac{\partial\psi}{\partial r} \end{aligned} \quad (5)$$

The non-zero linearized strains can be computed from the strain-displacement relations:

$$\begin{aligned} \varepsilon_{rr} &= \frac{\partial u_r}{\partial r} \\ \varepsilon_{\theta\theta} &= \frac{1}{r}\frac{\partial u_\theta}{\partial\theta} + \frac{u_r}{r} \\ \varepsilon_{r\theta} &= \frac{1}{2}\left(\frac{1}{r}\frac{\partial u_r}{\partial\theta} + \frac{\partial u_\theta}{\partial r} - \frac{u_\theta}{r}\right) \end{aligned} \quad (6)$$

and the linearized stresses can be computed from the linear elastic constitutive relations:

$$\begin{aligned} \sigma_{rr} &= 2\mu_i\varepsilon_{rr} + \lambda_i(\varepsilon_{rr} + \varepsilon_{\theta\theta}) \\ \sigma_{\theta\theta} &= 2\mu_i\varepsilon_{\theta\theta} + \lambda_i(\varepsilon_{rr} + \varepsilon_{\theta\theta}) \\ \sigma_{r\theta} &= 2\mu_i\varepsilon_{r\theta} \end{aligned} \quad (7)$$

2.2. Displacements and stresses in the matrix

Within the matrix, wave fields consist of incident and scattered waves. We study a planar harmonic compressional wave (P-wave) propagating in an arbitrarily chosen positive  $x$ -direction, which can be represented by the following potential in the  $x$ - $y$  plane (Pao and Mow, 1976):

$$\varphi^{(Inc)} = \varphi_0 e^{j(\alpha_1 x - \omega t)} \tag{8}$$

where the superscript (*Inc*) indicates the incident wave,  $\varphi_0$  is the amplitude of the wave function,  $\alpha_1 = \omega/c_{z1}$  is the wavenumber of the P-wave in the matrix,  $\omega$  is the circular frequency of the P-wave,  $t$  denotes time, and  $j = \sqrt{-1}$ .

In anticipation of writing the boundary conditions in cylindrical coordinates, the displacement potential of the incident wave may be expressed as (Pao and Mow, 1976):

$$\varphi^{(Inc)} = \varphi_0 \sum_{n=0}^{\infty} k_n i^n J_n(\alpha_1 r) \cos(n\theta) e^{-j\omega t} \tag{9}$$

where  $J_n(x)$  denotes the  $n$ th order Bessel function of the first kind and the Neumann factor  $k_n$  is  $k_0 = 1, k_n = 2(n \geq 1)$ .

Substituting Eq. (9) into Eq. (5) and Eq. (6), and then into Eq. (7), one obtains expressions for the displacements and stresses due to the incident wave as:

$$u_{r1}^{(Inc)} = \frac{\varphi_0}{r} \sum_{n=0}^{\infty} k_n i^n [\alpha_1 r J_{n-1}(\alpha_1 r) - n J_n(\alpha_1 r)] \cos(n\theta) e^{-j\omega t} \tag{10}$$

$$u_{\theta 1}^{(Inc)} = \frac{\varphi_0}{r} \sum_{n=0}^{\infty} k_n i^n [-n J_n(\alpha_1 r)] \sin(n\theta) e^{-j\omega t} \tag{11}$$

$$\sigma_{rr1}^{(Inc)} = \frac{2\mu_1 \varphi_0}{r^2} \sum_{n=0}^{\infty} k_n i^n [(n^2 + n - \beta_1^2 r^2 / 2) J_n(\alpha_1 r) - \alpha_1 r J_{n-1}(\alpha_1 r)] \cos(n\theta) e^{-j\omega t} \tag{12}$$

$$\sigma_{r\theta 1}^{(Inc)} = \frac{2\mu_1 \varphi_0}{r^2} \sum_{n=0}^{\infty} k_n i^n [n(n+1) J_n(\alpha_1 r) - n\alpha_1 r J_{n-1}(\alpha_1 r)] \sin(n\theta) e^{-j\omega t} \tag{13}$$

Due to mode conversion, the incident P-wave gives rise to scattered wave fields of two genera when it impinges upon the coated fiber: a scattered P-wave, and a vertical, polarized shear wave (SV-wave). The displacement potentials of these two scattered wave fields in the elastic medium can be expressed by (Pao and Mow, 1976)

$$\varphi^{(s)} = \varphi_0 \sum_{n=0}^{\infty} k_n i^n A_n H_n^{(1)}(\alpha_1 r) \cos(n\theta) e^{-j\omega t} \tag{14}$$

$$\psi^{(s)} = \varphi_0 \sum_{n=0}^{\infty} k_n i^n B_n H_n^{(1)}(\beta_1 r) \sin(n\theta) e^{-j\omega t} \tag{15}$$

where  $H_n^{(1)}(x)$  is the  $n$ th order Hankel function of the first kind,  $\beta_1 = \omega/c_{\beta 1}$  is the wavenumber of the shear wave,  $A_n$  and  $B_n$  are unknown constants to be determined using boundary conditions, and the superscript (*s*) indicates the scattered waves.

Substitution of (14) and (15) firstly into (5) and (6) and then into (7) leads to the expressions for displacements and stresses in the matrix due to wave scattering:

$$u_{r1}^{(s)} = \frac{\varphi_0}{r} \sum_{n=0}^{\infty} k_n i^n \{A_n [\alpha_1 r H_{n-1}(\alpha_1 r) - n H_n(\alpha_1 r)] + B_n [n H_n(\beta_1 r)]\} \cos(n\theta) e^{-j\omega t} \tag{16}$$

$$u_{\theta 1}^{(s)} = \frac{\varphi_0}{r} \sum_{n=0}^{\infty} k_n i^n \left\{ \begin{array}{l} A_n [-n H_n^{(1)}(\alpha_1 r)] + \\ B_n [-\beta_1 r H_{n-1}^{(1)}(\beta_1 r) + n H_n^{(1)}(\beta_1 r)] \end{array} \right\} \sin(n\theta) e^{-j\omega t} \tag{17}$$

$$\sigma_{rr1}^{(s)} = \frac{2\mu_1 \varphi_0}{r^2} \sum_{n=0}^{\infty} k_n i^n \left\{ \begin{array}{l} A_n \left[ \begin{array}{l} (n^2 + n - \beta_1^2 r^2 / 2) H_n^{(1)}(\alpha_1 r) \\ -\alpha_1 r H_{n-1}^{(1)}(\alpha_1 r) \end{array} \right] \\ + B_n \left[ \begin{array}{l} -n(n+1) H_n^{(1)}(\beta_1 r) \\ +n\beta_1 r H_{n-1}^{(1)}(\beta_1 r) \end{array} \right] \end{array} \right\} \cos(n\theta) e^{-j\omega t} \tag{18}$$

$$\sigma_{r\theta 1}^{(s)} = \frac{2\mu_1 \varphi_0}{r^2} \sum_{n=0}^{\infty} k_n i^n \left\{ \begin{array}{l} A_n \left[ \begin{array}{l} n(n+1) H_n^{(1)}(\alpha_1 r) \\ -n\alpha_1 r H_{n-1}^{(1)}(\alpha_1 r) \end{array} \right] \\ + B_n \left[ \begin{array}{l} -(n^2 + n - \beta_1^2 r^2 / 2) H_n^{(1)}(\beta_1 r) \\ +\beta_1 r H_{n-1}^{(1)}(\beta_1 r) \end{array} \right] \end{array} \right\} \sin(n\theta) e^{-j\omega t} \tag{19}$$

The total displacement and stress fields in the matrix are obtained by superposition of contributions due to incident and scattered waves.

2.3. Displacements and stresses in the coating

Displacement potentials for refracted, standing waves confined within the coating can be expressed as (Pao and Mow, 1976):

$$\varphi_2 = \varphi_0 \sum_{n=0}^{\infty} k_n i^n [C_n H_n^{(1)}(\alpha_2 r) + D_n H_n^{(2)}(\alpha_2 r)] \cos(n\theta) e^{-j\omega t} \tag{20}$$

$$\psi_2 = \varphi_0 \sum_{n=0}^{\infty} k_n i^n [M_n H_n^{(1)}(\beta_2 r) + N_n H_n^{(2)}(\beta_2 r)] \sin(n\theta) e^{-j\omega t} \tag{21}$$

where  $H_n^{(2)}(x)$  is the  $n$ th order Hankel function of the second kind, and  $C_n, D_n, M_n$  and  $N_n$  are constants to be determined from boundary conditions.

By substituting (20) and (21) firstly into (5) and (6) and then into (7), expressions for the displacements and stresses due to the refracted waves can be determined as:

$$u_{r2} = \frac{\varphi_0}{r} \sum_{n=0}^{\infty} k_n i^n \left\{ \begin{array}{l} C_n [\alpha_2 r H_{n-1}^{(1)}(\alpha_2 r) - n H_n^{(1)}(\alpha_2 r)] \\ + D_n [\alpha_2 r H_{n-1}^{(2)}(\alpha_2 r) - n H_n^{(2)}(\alpha_2 r)] \\ + M_n [n H_n^{(1)}(\beta_2 r)] + N_n [n H_n^{(2)}(\beta_2 r)] \end{array} \right\} \cos(n\theta) e^{-j\omega t} \tag{22}$$

$$u_{\theta 2} = \frac{\varphi_0}{r} \sum_{n=0}^{\infty} k_n i^n \left\{ \begin{array}{l} C_n [-n H_n^{(1)}(\alpha_2 r)] + D_n [-n H_n^{(2)}(\alpha_2 r)] \\ + M_n [-\beta_2 r H_{n-1}^{(1)}(\beta_2 r) + n H_n^{(1)}(\beta_2 r)] \\ + N_n [-\beta_2 r H_{n-1}^{(2)}(\beta_2 r) + n H_n^{(2)}(\beta_2 r)] \end{array} \right\} \sin(n\theta) e^{-j\omega t} \tag{23}$$

$$\sigma_{rr2} = \frac{2\mu_2 \varphi_0}{r^2} \sum_{n=0}^{\infty} k_n i^n \left\{ \begin{array}{l} C_n [(n^2 + n - \beta_2^2 r^2 / 2) H_n^{(1)}(\alpha_2 r)] \\ + D_n [(n^2 + n - \beta_2^2 r^2 / 2) H_n^{(2)}(\alpha_2 r)] \\ + M_n [-n(n+1) H_n^{(1)}(\beta_2 r) + n\beta_2 r H_{n-1}^{(1)}(\beta_2 r)] \\ + N_n [-n(n+1) H_n^{(2)}(\beta_2 r) + n\beta_2 r H_{n-1}^{(2)}(\beta_2 r)] \end{array} \right\} \cos(n\theta) e^{-j\omega t} \tag{24}$$

$$\sigma_{r\theta 2} = \frac{2\mu_2 \varphi_0}{r^2} \sum_{n=0}^{\infty} k_n i^n \left\{ \begin{array}{l} C_n [n(n+1) H_n^{(1)}(\alpha_2 r) - n\alpha_2 r H_{n-1}^{(1)}(\alpha_2 r)] \\ + D_n [n(n+1) H_n^{(2)}(\alpha_2 r) - n\alpha_2 r H_{n-1}^{(2)}(\alpha_2 r)] \\ + M_n \left[ \begin{array}{l} -(n^2 + n - \beta_2^2 r^2 / 2) H_n^{(1)}(\beta_2 r) \\ +\beta_2 r H_{n-1}^{(1)}(\beta_2 r) \end{array} \right] \\ + N_n \left[ \begin{array}{l} -(n^2 + n - \beta_2^2 r^2 / 2) H_n^{(2)}(\beta_2 r) \\ +\beta_2 r H_{n-1}^{(2)}(\beta_2 r) \end{array} \right] \end{array} \right\} \sin(n\theta) e^{-j\omega t} \tag{25}$$

### 2.4. Displacements and stresses in the fiber

The longitudinal and shear waves transmitted into the cylindrical elastic fiber are also standing refracted waves, and can be written in the following form (Pao and Mow, 1976):

$$\varphi_3 = \varphi_0 \sum_{n=0}^{\infty} k_n i^n F_n J_n(\alpha_3 r) \cos(n\theta) e^{-j\omega t} \quad (26)$$

$$\psi_3 = \varphi_0 \sum_{n=0}^{\infty} k_n i^n G_n J_n(\beta_3 r) \sin(n\theta) e^{-j\omega t} \quad (27)$$

The displacement field in the fiber is obtained by substituting (26) and (27) into (5):

$$u_{r3} = \frac{\varphi_0}{r} \sum_{n=0}^{\infty} k_n i^n \{F_n[\alpha_3 r J_n(\alpha_3 r) - n J_n(\alpha_3 r)] + G_n[n J_n(\beta_3 r)]\} \cos(n\theta) e^{-j\omega t} \quad (28)$$

$$u_{\theta 3} = \frac{\varphi_0}{r} \sum_{n=0}^{\infty} k_n i^n \{F_n[-n J_n(\alpha_3 r)] + G_n[-\beta_3 r J_{n-1}(\beta_3 r) + n J_n(\beta_3 r)]\} \sin(n\theta) e^{-j\omega t} \quad (29)$$

Similarly, the stress field is obtained by substituting (28) and (29) into (6) and then into (7), as:

$$\sigma_{rr3} = \frac{2\mu_3 \varphi_0}{r^2} \sum_{n=0}^{\infty} k_n i^n \left\{ \begin{array}{l} F_n \left[ \begin{array}{l} (n^2 + n - \beta_3^2 r^2 / 2) J_n(\alpha_3 r) \\ -\alpha_3 r J_{n-1}(\alpha_3 r) \\ + G_n \left[ \begin{array}{l} -n(n+1) J_n(\beta_3 r) \\ + n \beta_3 r J_{n-1}(\beta_3 r) \end{array} \right] \end{array} \right] \end{array} \right\} \cos(n\theta) e^{-j\omega t} \quad (30)$$

$$\sigma_{\theta\theta 3} = \frac{2\mu_3 \varphi_0}{r^2} \sum_{n=0}^{\infty} k_n i^n \left\{ \begin{array}{l} F_n \left[ \begin{array}{l} n(n+1) J_n(\alpha_3 r) \\ -n \alpha_3 r J_{n-1}(\alpha_3 r) \\ + G_n \left[ \begin{array}{l} -(n^2 + n - \beta_3^2 r^2 / 2) J_n(\beta_3 r) \\ + \beta_3 r J_{n-1}(\beta_3 r) \end{array} \right] \end{array} \right] \end{array} \right\} \sin(n\theta) e^{-j\omega t} \quad (31)$$

### 2.5. Boundary conditions

The unknown coefficients appearing in the displacement potentials are determined by the boundary conditions, which enforce continuity of displacements and stresses at the matrix/coating/fiber interfaces:

$$u_{r1}^{(inc)} + u_{r1}^{(s)} = u_{r2}, u_{\theta 1}^{(inc)} + u_{\theta 1}^{(s)} = u_{\theta 2}, \quad (32)$$

$$\sigma_{rr1}^{(inc)} + \sigma_{rr1}^{(s)} = \sigma_{rr2}, \sigma_{r\theta 1}^{(inc)} + \sigma_{r\theta 1}^{(s)} = \sigma_{r\theta 2} \text{ at } r = b$$

$$u_{r2} = u_{r3}, u_{\theta 2} = u_{\theta 3}, \sigma_{rr2} = \sigma_{rr3}, \sigma_{r\theta 2} = \sigma_{r\theta 3} \text{ at } r = a$$

Substitution of the expressions for displacements and stresses into (32) and making use of the orthogonality of transcendental functions leads to, for  $n \geq 0$ , a set of simultaneous algebraic equations that can be expressed in matrix form as:

$$[Q]\{X_n\} = \{f\} \quad (33)$$

where the vector  $\{X_n\}$  contains the unknown coefficients  $A_n, B_n, C_n, D_n$  etc. The elements of  $[Q]$  and  $\{f\}$  are complex valued. One can obtain the unknown coefficients by solving Eq. (33).

For dynamic loading by the incident P-wave defined in Eq. (8) through an isotropic, linear elastic medium without fiber reinforcement, the stress field in the medium can be expressed in Cartesian coordinates as (Pao et al., 1973):

$$\sigma_{xx} = -(\lambda_1 + 2\mu_1) \alpha_1^2 \varphi_0 e^{j(\alpha_1 x - \omega t)} \quad (34)$$

$$\sigma_{yy} = -\lambda_1 \alpha_1^2 \varphi_0 e^{j(\alpha_1 x - \omega t)} \quad (35)$$

$$\sigma_{zz} = 2\nu_1 (\lambda_1 + \mu_1) \alpha_1^2 \varphi_0 e^{j(\alpha_1 x - \omega t)} \quad (36)$$

where  $\nu_1$  denotes the Poisson ratio of the matrix. All shear stresses vanish and the maximum stress is  $\sigma_0 = (\lambda_1 + 2\mu_1) \alpha_1^2 \varphi_0 = \mu_1 \beta_1^2 \varphi_0$ .

The solution procedure is valid only up to the point at which plastic flow occurs. Although the conditions for plastic flow in response to short duration stress waves can differ from conditions associated with quasistatic loading, the von Mises yield criterion is a reasonable first approximation for most metals. Thus, coatings are favorable if they reduce the von Mises equivalent stress, which can be written in our cylindrical coordinate system as:

$$\sigma_{vm} = \frac{1}{\sqrt{2}} \left[ (\sigma_{rr} - \sigma_{\theta\theta})^2 + (\sigma_{rr} - \sigma_{zz})^2 + (\sigma_{zz} - \sigma_{\theta\theta})^2 + 6(\sigma_{r\theta}^2 + \sigma_{rz}^2 + \sigma_{\theta z}^2) \right]^{1/2} \quad (37)$$

For convenience, we normalize stresses by the magnitude of incident stress  $\sigma_0$  in a homogeneous matrix and the associated von Mises equivalent stress  $\sigma'_0$ , as:

$$\sigma_{kl}^* = \frac{|\sigma_{kl}|}{\sigma_0}, k, l = r, \theta \quad (38)$$

$$\sigma_{vm}^* = \frac{|\sigma_{vm}|}{\sigma'_0} \quad (39)$$

where

$$\sigma'_0 = \frac{1 - 2\nu_1}{1 - \nu_1} \mu_1 \beta_1^2 \varphi_0 \quad (40)$$

the latter of which can be obtained by inserting (34)–(36) into (37).  $\sigma_{kl}^*$  and  $\sigma_{vm}^*$  represent dynamic stress concentration factors (DSCFs) due to the presence of fibers or coated fibers.

Further examination of (38) and (39) shows that these dimensionless stresses depend upon the coating thickness, the dimensionless incident wave frequency,  $\omega^*$ , and three additional dimensionless parameters: (1) the ratio of shear modulus of coating and matrix,  $\mu_2/\mu_1$ ; (2) the ratio of density of coating and matrix,  $\rho_2/\rho_1$ ; (3) the Poisson ratio of the coating,  $\nu_2$ . In the following parametric study, we characterized how dynamic stresses were affected by the coating thickness and these dimensionless parameters. Computations proceeded by first solving Eq. (33) with the specific boundary conditions (Eq. (32)) to compute the scattering coefficient  $\{X_n\}$ , and its unknown coefficients, including  $A_n$  and  $B_n$ .  $A_n$  and  $B_n$  were then incorporated into Eqs. (16) and (17) to obtain the displacement field in the matrix. Finally, by inserting these into the strain–displacement and constitutive relations (Eqs. (6) and (7)), we computed the stresses in the matrix, then computed the stress at the interface by setting  $r = b$ . The von Mises equivalent stress was then obtained by inserting the stress components into Eq. (37), and the normalized stress was obtained using Eqs. (38) and (39). All calculations were performed using Matlab (The Mathworks, Natick, MA).

### 2.6. Transient waves

To assess how coatings affect the response to transient loading, we studied an incident wave on the coated fiber-reinforced composite material subjected to a transient pulse. The form of this pulse was chosen to represent a blast wave, which characteristically presents a relatively short rise time and a relatively longer decay time. Following others (Wang et al., 2017), we represented this with a needle wave function that combines sine and exponential functions. This function can be expressed as  $P(t) = P_{max} f(t)$ , in which  $P_{max}$  is the peak impact pressure and  $f(t)$  follows (Fig. 2):

$$f(t) = e^{\xi \tan^{-1}(\frac{t}{\eta})} \sqrt{1 + (\frac{\xi}{\eta})^2} \cdot e^{-\xi t} \sin \eta t \quad t \in [0, T_2] \tag{41}$$

For  $t < 0$  or  $t > T_2$ ,  $f(t) = 0$ . Defining  $\eta = \pi/T_2$  and  $f(T_1)$  as the maximum value, we write:

$$\xi = \eta \cot \eta T_1 = (\pi/T_2) \cot(\pi T_1/T_2) \tag{42}$$

The transient wave requires one period to reach its peak value at time  $T_1$  then decrease more gradually to 0 at time  $T_2$  (Fig. 2).

For our study,  $t = 0$  when the transient wave impinges on the coating boundary. For calculation, we normalized the time  $t$  by the time needed to travel through the inclusion as

$$\tau = \frac{c_1 t}{b} \tag{43}$$

Thus the normalized  $T_1$  can be expressed as  $\tau_1 = c_1 T_1/b$ . Dynamic stresses for the continuous wave can be expressed as

$$\frac{\sigma_{kl}}{\sigma_0} = R(\omega) + iI(\omega) \tag{44}$$

We applied a Fourier transform technique to bridge the steady state and transient responses. The transient wave (Eq. (41)) meets the Dirichlet conditions and is integrable, so the transient response of the system can be expressed as (Pao and Mow, 1976):

$$g(x_i, t) = \frac{1}{\sqrt{2\pi}} \int_{-\infty}^{\infty} \chi(x_i, t) F(\omega) e^{-i\omega t} d\omega \tag{45}$$

where  $\chi(x_i, t)$  is the admittance function defined as the steady state response of the system under a unit magnitude force, and  $F(\omega)$  is the Fourier transformed form of input function  $f(t)$ .

Because we focus on the dynamic stress response in the matrix around the inclusion, the normalized dynamic stresses  $\sigma_{kl}/\sigma_0$  can work as the admittance function. Because  $f(t) = 0$  for  $t < 0$ , the response  $g(x_i, t)$  can alternatively be expressed in terms as sine or cosine transforms. Furthermore, to reduce the computational complexity, the  $\delta(t)$  function and Heaviside step function were used (Pao and Mow, 1976). The Fourier transform of  $\delta(t)$  is

$$\frac{1}{\sqrt{2\pi}} \int_{-\infty}^{\infty} \delta(t) e^{-i\omega t} dt = \frac{1}{\sqrt{2\pi}} \tag{46}$$

Therefore, the dynamic response caused by the  $\delta(t)$  function can be expressed as (Pao and Mow, 1976)

$$g_\delta(x_i, t) = \frac{2}{\pi} \int_0^\infty R(\omega) \cos \omega t d\omega = \frac{2}{\pi} \int_0^\infty I(\omega) \sin \omega t d\omega \tag{47}$$

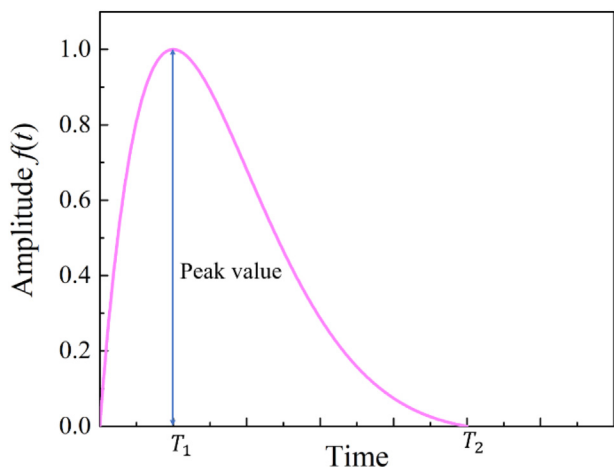


Fig. 2. Transient loading curve.

Then, the response of Heaviside step function can be expressed by the impulse response as (Pao and Mow, 1976)

$$g_h(x_i, t) = \int_0^t g_\delta(x_i, \tau) d\tau = \frac{2}{\pi} \int_0^\infty \frac{R(\omega) \sin \omega t}{\omega} d\omega \tag{48}$$

According to the Duhamel integral, for arbitrary input function  $f(\tau)$ , the transient response can be written (Pao and Mow, 1976):

$$g(x_i, t) = \int_0^t f(\tau) g_h'(t - \tau) d\tau = f(0)g_h(t) + \int_0^t f'(\tau)g_h(t - \tau) d\tau \tag{49}$$

Therefore, for the needle shape transient wave we studied here, when  $0 \leq t \leq T_2$ , we have

$$g(x_i, t) = \frac{2}{\pi} \int_0^\infty \int_0^t e^{-\tau\xi + \frac{\xi}{\eta} \tan^{-1}(\frac{\tau}{\eta})} \times \sqrt{1 + \frac{\xi^2}{\eta^2}} [\eta \cos(\tau\eta) - \xi \sin(\tau\eta)] \frac{R(\omega) \sin[\omega(t - \tau)]}{\omega} d\tau d\omega = \int_0^\infty \frac{-2e^{-\tau\xi + \frac{\xi}{\eta} \tan^{-1}(\frac{\tau}{\eta})} R(\omega) \sqrt{1 + \frac{\xi^2}{\eta^2}}}{\pi [\xi^2 + (\eta - \omega)^2] [\xi^2 + (\eta + \omega)^2]} \times \left\{ \begin{array}{l} \eta(\xi^2 + \eta^2 - \omega^2) \cos(\eta t) \\ + \xi(\xi^2 + \eta^2 + \omega^2) \sin(\eta t) \\ - e^{\xi t} \eta \left[ \begin{array}{l} (\xi^2 + \eta^2 - \omega^2) \cos(\omega t) \\ + 2\xi\omega \sin(\omega t) \end{array} \right] \end{array} \right\} d\omega \tag{50}$$

when  $t > T_2$ , we have

$$g(x_i, t) = \frac{2}{\pi} \int_0^\infty \int_0^{T_2} e^{-\tau\xi + \frac{\xi}{\eta} \tan^{-1}(\frac{\tau}{\eta})} \times \sqrt{1 + \frac{\xi^2}{\eta^2}} [\eta \cos(\tau\eta) - \xi \sin(\tau\eta)] \frac{R(\omega) \sin[\omega(t - \tau)]}{\omega} d\tau d\omega = \left\{ \begin{array}{l} \int_0^\infty \frac{-2e^{-T_2\xi + \frac{\xi}{\eta} \tan^{-1}(\frac{T_2}{\eta})} R(\omega) \sqrt{1 + \frac{\xi^2}{\eta^2}}}{\pi [\xi^2 + (\eta - \omega)^2] [\xi^2 + (\eta + \omega)^2]} \\ \sin(\omega t) \left[ \begin{array}{l} -2e^{T_2\xi} \xi \eta \omega^2 + \eta \omega \cos(T_2\eta) \left[ \begin{array}{l} 2\xi\omega \cos(T_2\omega) + \\ (\xi^2 + \eta^2 - \omega^2) \sin(T_2\omega) \end{array} \right] \\ \sin(T_2\eta) \left[ \begin{array}{l} -[(\xi^2 + \eta^2)^2 + (\xi^2 - \eta^2)\omega^2] \cos(T_2\omega) \\ + \xi\omega(\xi^2 + \eta^2 + \omega^2) \sin(T_2\omega) \end{array} \right] \end{array} \right] \\ \cos(\omega t) \left[ \begin{array}{l} -e^{T_2\xi} \eta \omega (\xi^2 + \eta^2 - \omega^2) \\ + \eta \omega \cos(T_2\eta) \left[ \begin{array}{l} (\xi^2 + \eta^2 - \omega^2) \cos(T_2\omega) \\ - 2\xi\omega \sin(T_2\omega) \end{array} \right] \\ + \sin(T_2\eta) \left( \begin{array}{l} \xi\omega(\xi^2 + \eta^2 + \omega^2) \cos(T_2\omega) \\ [(\xi^2 + \eta^2)^2 + (\xi^2 - \eta^2)\omega^2] \sin(T_2\omega) \end{array} \right) \end{array} \right] \end{array} \right\} d\omega \tag{51}$$

Based on Eqs. (50) and (51), we studied the transient stress behavior of fiber reinforced composite materials. Eqs. (50) and (51) were evaluated numerically using trapezoidal functions by determining  $R(\omega)$  from the real part of  $\sigma_{kl}^*/\sigma_0$  or  $\sigma_{vm}^*/\sigma_0$ , found as described above for the case of continuous waves.

### 3. Results and discussion

We studied, as a model problem, a titanium alloy matrix composite material, with parameters as shown in Table 1. We studied

**Table 1**  
Material properties of fiber reinforced composite phases (Leão-Neto et al., 2017).

Material	Young's modulus (GPa)	Poisson's ratio	Density (kg/m <sup>3</sup> )
Fiber (carbon)	41	0.25	1700
Matrix (Ti alloy)	121.6	0.348	5400

a range of coatings representing the properties of BN, graphite (Bogan and Hinders, 1993), pyrolytic carbon (Carman et al., 1993), ZrO<sub>2</sub> (He et al., 2019), and Al<sub>2</sub>O<sub>3</sub> (Verbis et al., 2002). The

dimensionless quantities studied were thus  $\mu_2/\mu_1 = 0.8, 1.2, 1.6, 2$ ,  $\rho_2/\rho_1 = 0.8, 1.2, 1.6, 2$ , and  $\nu_2 = 0.2, 0.3, 0.4, 0.45$ . Although these values do not cover the range of parameters possible for practical applications, they demonstrated the influence of coatings on dynamic stress concentrations.

### 3.1. Static comparison case and dynamic stress amplification

For comparison, we investigated the limiting static case for an incident P-wave whose wavelength is infinite ( $\alpha_1 \rightarrow 0$ ). For this,

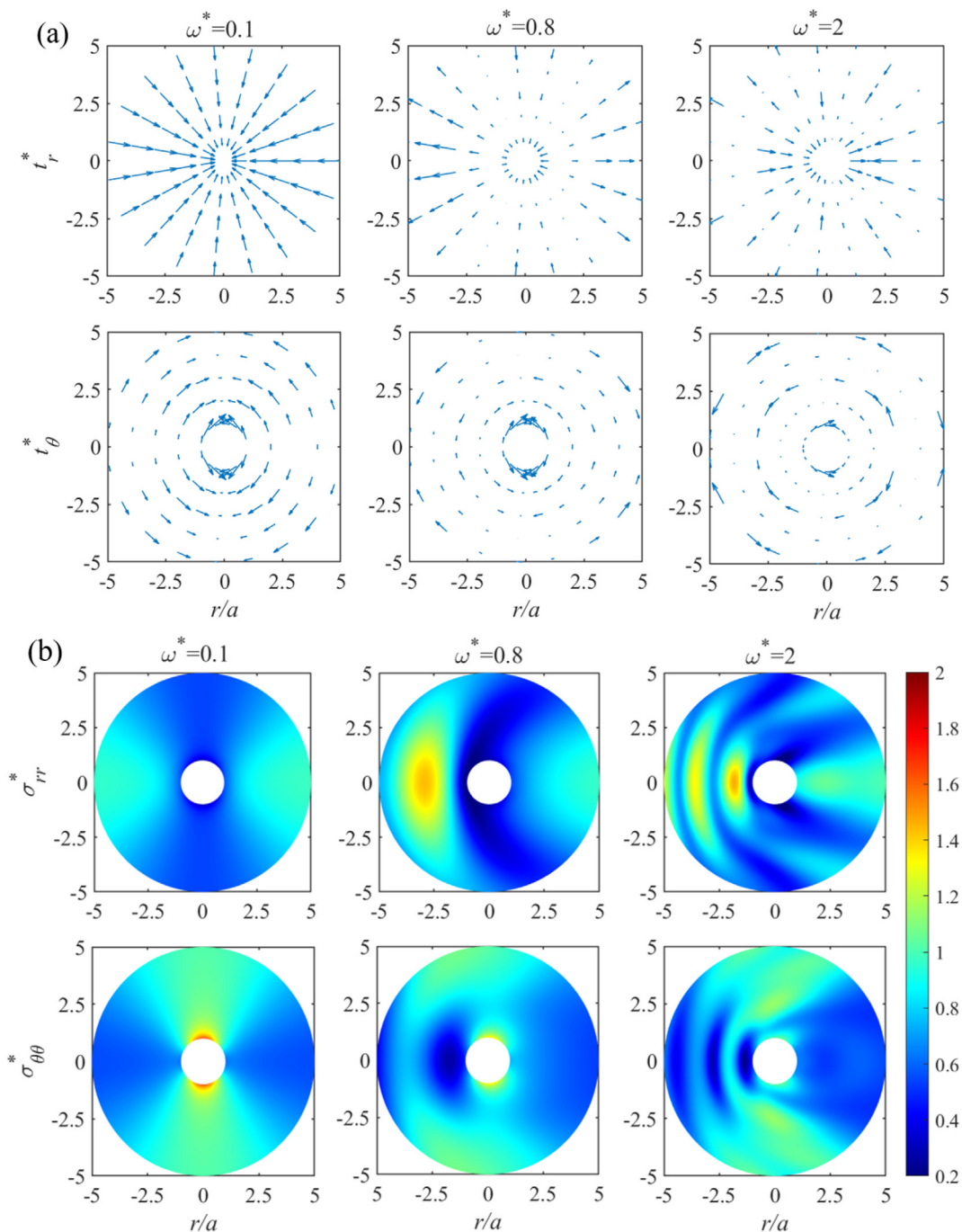


**Fig. 3.** (a) Traction vector field in the matrix around the fiber. (b) Stress distribution around fiber without a coating at relatively low and high frequencies for an incident P-wave approaching from the left side. The fields are symmetric with respect to the horizontal axis. Contours represent the range of normalized dynamic stress.

the solutions obtained using the current approach should asymptotically approach the static case:

$$\begin{aligned} \sigma_{xx} &= -\sigma_0 \\ \sigma_{yy} &= -\frac{\lambda_1}{\lambda_1 + 2\mu_1} \sigma_0 \\ \sigma_{zz} &= \frac{2\nu_1(\lambda_1 + \mu_1)}{\lambda_1 + 2\mu_1} \sigma_0 \end{aligned} \tag{52}$$

with shear stresses 0. The stress field of (52) is triaxial and hence the results presented below are for the dynamic counterparts of these fields. Stress fields in the absence of a coating the stresses were expressed as infinite series using Eqs. (12), (13), (18) and (19). To ensure convergence, the series were truncated at  $n = N$  using the Wiscombe criterium (Mahmoudian and Margrave, 2007):

$$N = \lceil \omega^* + 4.05(\omega^*)^{1/3} + 2 \rceil \tag{53}$$

where  $\lceil x \rceil$  represents the nearest integer to  $x$ , and  $\omega^* = \alpha_1 b$  is the normalized frequency.

In the absence of a fiber coating, normalized stresses  $\sigma_{rr}^*$  and  $\sigma_{\theta\theta}^*$  within the matrix were sensitive to the frequency of a harmonic incident P-wave (Fig. 3). The traction vector was plotted and all of them are symmetric with respect to the horizontal axis (Fig. 3a). Scattering affected the stress most within a few radii the cylindrical fiber, with the scattered wave amplitude decreasing with distance from the fiber and approaching zero at infinity. At lower frequencies, for which  $\lambda = 2\pi/\alpha_1 = 20\pi b$  was far larger than the radius of the fiber, the stresses arising from a harmonic incident wave resembled those of a quasi-static loading, with symmetry about the vertical axis for a wave arriving in the horizontal direction (e.g.,  $\omega^* = 0.1$ , Fig. 3b). In this case, at the fiber/matrix interface, the maximum value of  $\sigma_{rr}^*$  occurred at  $\theta = 0$  and  $\theta = \pi$  while the maximum value of  $\sigma_{\theta\theta}^*$  occurred at  $\theta = \pm\pi/2$ .

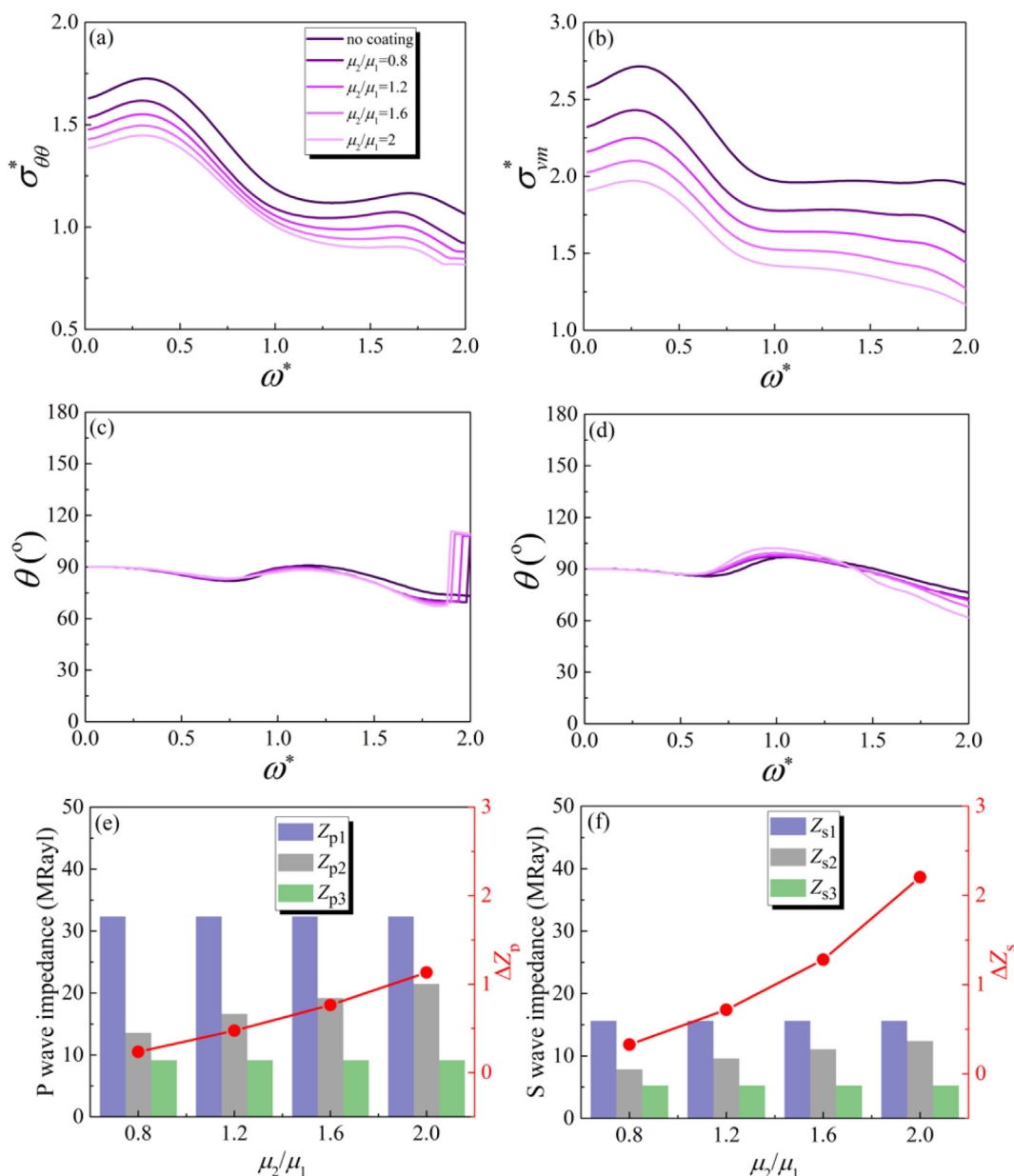


**Fig. 4.** (a) Normalized hoop stress  $\sigma_{\theta\theta}^*$  and (b) von Mises stress  $\sigma_{vm}^*$  plotted as a function of normalized frequency  $\omega^*$  for selected values of coating shear modulus  $\mu_2/\mu_1$ , with the density and Poisson ratio of the coating held constant and equal to those of the fiber ( $\rho_2 = \rho_3$  and  $\nu_2 = \nu_3$ ). (c) Angular location of the maximum hoop stress and (d) von Mises stress for different coating shear modulus ratios  $\mu_2/\mu_1$ , under these same conditions. (e) P wave impedances and (f) S wave impedances plotted for selected values of coating shear modulus ratio  $\mu_2/\mu_1$ .

For higher frequency incident waves (e.g.,  $\omega^* = 2$ , Fig. 3b), dynamic loading effects arising from reflection, refraction and scattering of the incident were evident as deviations from the quasi-static solution. The normalized radial stress  $\sigma_{rr}^*$  became more concentrated on the illuminated side of the fiber near the fiber/matrix interface. A ripple effect, absent from the quasi-static case, emerged in the incident region due to scattering. Scattering broke the symmetry of the normalized hoop stress ( $\sigma_{\theta\theta}^*$ ) distribution. Normalized stresses were always maximal at the interface between the fiber and matrix, consistent with the observation that in many practical applications of fiber reinforced composite materials, failure is often initiated in the matrix at the interface between the fiber and matrix.

### 3.2. Effects of coatings on dynamic stress concentrations for steady state waves

The influence of a coating on dynamic stress concentrations was studied by first considering coatings with a fixed thickness of  $0.1a$ . For a given frequency, dynamic stress concentrations in the matrix were obtained by calculating the normalized stress components as a function of angle and searching for the maximum value for  $\omega^*$  in the range of 0–2 (Fig. 4).

In the comparison case without a coating, the normalized circumferential and von Mises stresses increased with normalized frequencies up to  $\omega^* = 0.4$ , then decreased to a plateau that was interrupted by minor oscillations before decreasing further

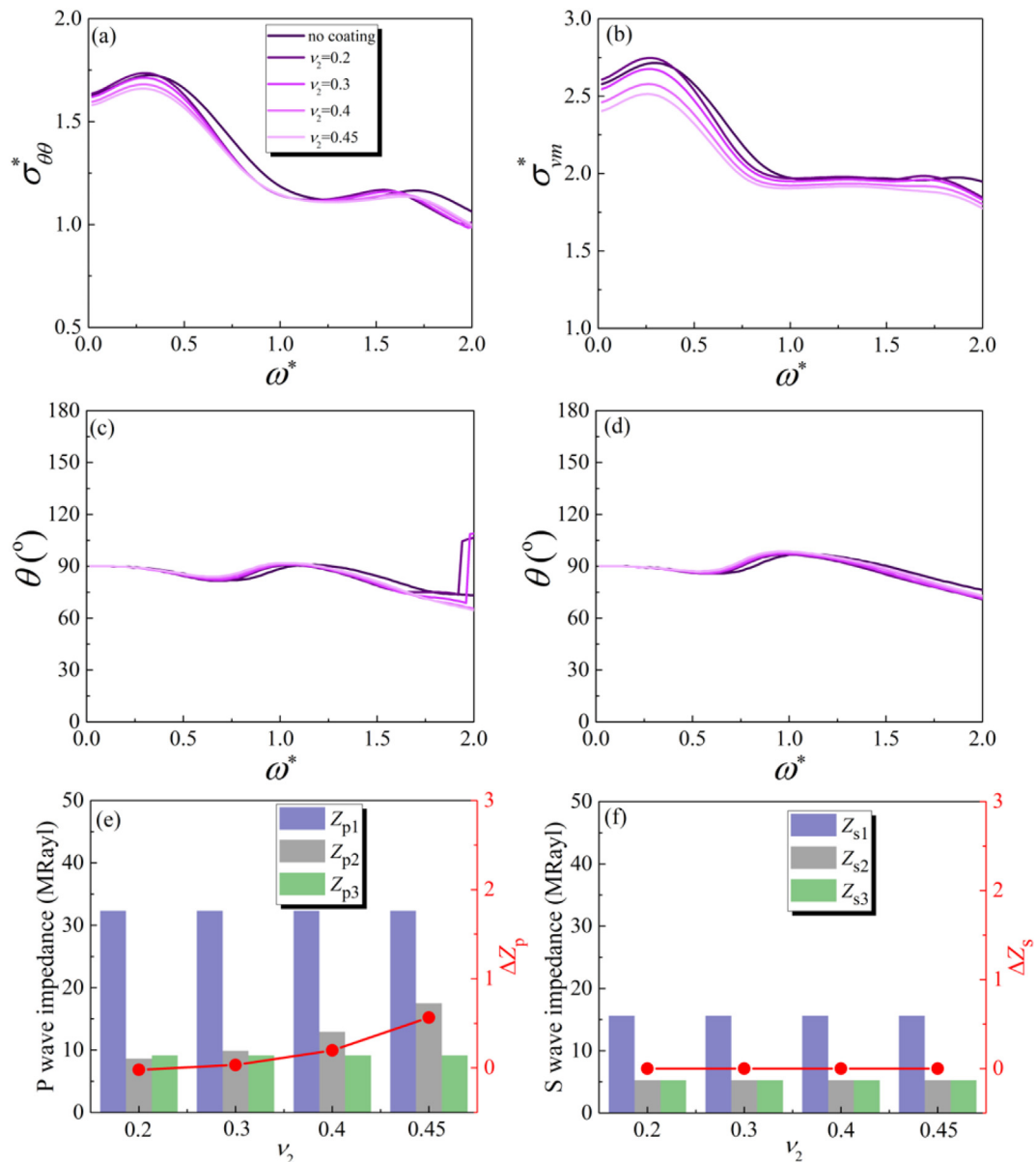


**Fig. 5.** (a) Normalized hoop stress  $\sigma_{\theta\theta}$  and (b) von Mises stress  $\sigma_{vm}^*$  plotted as a function of normalized frequency  $\omega^*$  for selected values of coating Poisson ratio  $\nu_2$ , with the density and shear modulus of the coating held constant and equal to those of the fiber ( $\rho_2 = \rho_3$  and  $\mu_2 = \mu_3$ ). (c) Angular location of the maximum hoop stress and (d) von Mises stress for different coating Poisson ratio  $\nu_2$ , under these same conditions. (e) P wave impedances and (f) S wave impedances plotted for selected values of coating Poisson ratio  $\nu_2$ .

(Fig. 4a and b). The angular locations of the maximum circumferential and von Mises stresses (Fig. 4c and d) were always near  $\theta = \pi/2$ . For the frequency range studied, peak dynamic stress concentration factors were always larger than 1, highlighting the significance of dynamic effects when designing advanced composite materials.

We next considered the effect of the coating shear modulus by varying the coating shear modulus while keeping constant the matrix and coating density and Poisson ratio,  $\rho_2 = \rho_3$  and  $\nu_2 = \nu_3$ .  $\sigma_{rr}^*$  was less than 1 for all cases (results not shown), with no stress amplification in the radial direction. Dynamic stress concentration factors were greater than 1 for both  $\sigma_{\theta\theta}^*$  and  $\sigma_{vm}^*$ , but decreased with coating shear modulus (Fig. 4a,b). The locations of the maximum stress were again near  $\theta = \pi/2$ . For some cases, for example  $\mu_2/\mu_1 = 2$  at  $1.8 < \omega^* < 2$ , a sharp transition point in  $\sigma_{\theta\theta}^*$  was evident due to a shift in the location of the angular loca-

tion of peak stress from  $68^\circ$  to  $111^\circ$  (Fig. 4c). These reductions of dynamic stress concentration could be further understood by studying scattering of the incident wave  $\varphi^{(inc)}$ . With  $\varphi^{(inc)}$  held constant, the scattered waves  $\varphi^{(s)}$  and  $\psi^{(s)}$  were influenced only by mismatches in the wave impedances of the scattered waves P- and S-waves, defined in material  $i$  as (Peng et al., 2020; Peng, 2020)

$$\begin{aligned} Z_{pi} &= \rho_i C_{zi} \\ Z_{si} &= \rho_i C_{\beta i} \end{aligned} \tag{54}$$

For the model composite studied, the matrix impedances,  $Z_{p1} = 32.3$  MRayl and  $Z_{s1} = 15.6$  MRayl, were much larger than their counterparts of the fiber, leading to a large wave impedance gradient. The coatings studied had P- and S-wave impedances between those of the matrix and fiber and were studied in terms

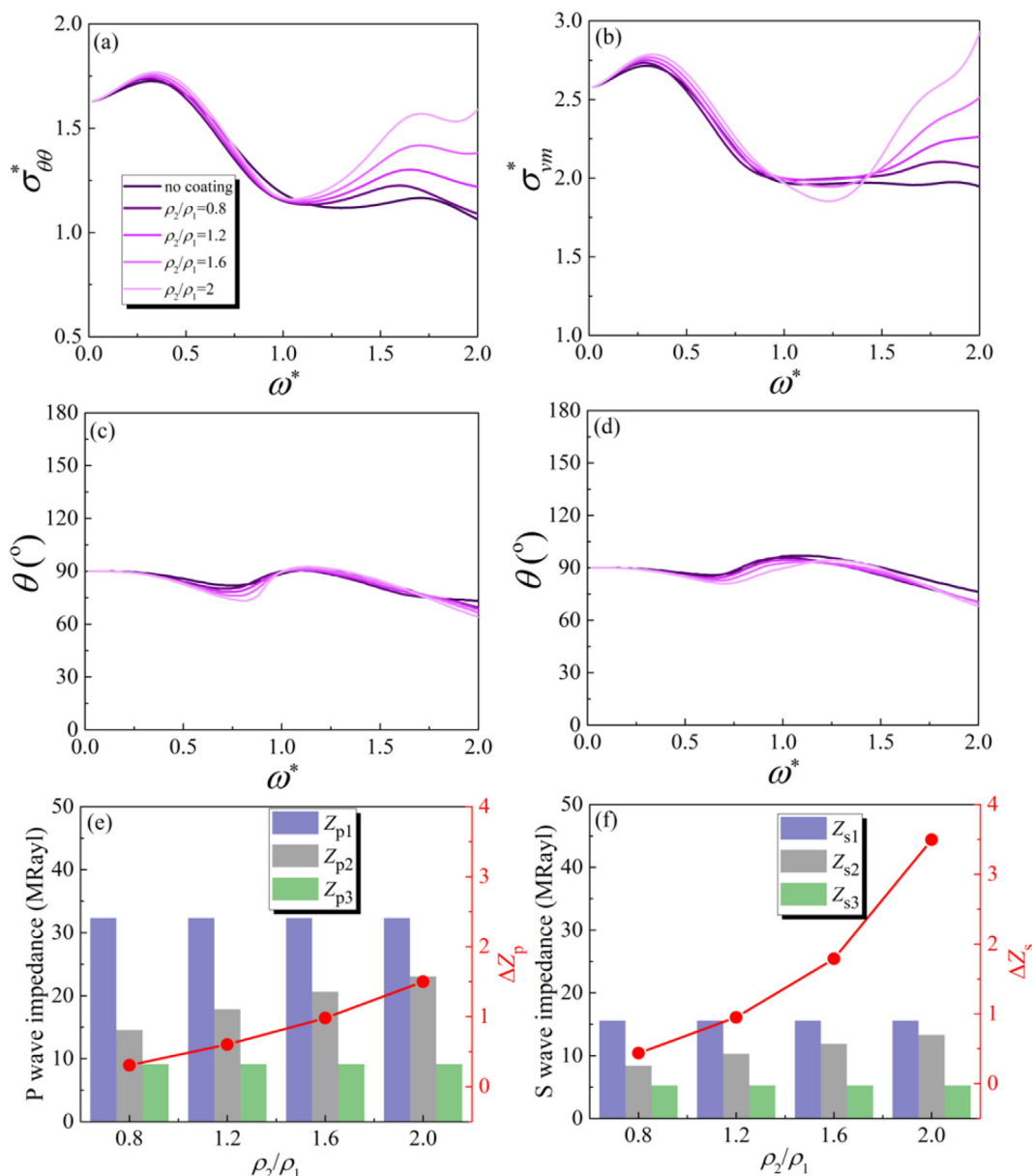


**Fig. 6.** (a) Normalized hoop stress  $\sigma_{\theta\theta}^*$  and (b) von Mises stress  $\sigma_{vm}^*$  plotted as a function of normalized frequency  $\omega^*$  for selected values of coating density  $\rho_2/\rho_1$ , with the Poisson ratio and shear modulus of the coating held constant and equal to those of the fiber ( $\nu_2 = \nu_3$  and  $\mu_2 = \mu_3$ ). (c) Angular location of the maximum hoop stress and (d) von Mises stress for different coating density  $\rho_2/\rho_1$ , under these same conditions. (e) P wave impedances and (f) S wave impedances plotted for selected values of coating density  $\rho_2/\rho_1$ .

of a relative wave impedance change, defined as the ratio of the mismatch between the coating and fiber to that between the matrix and coating:

$$\begin{aligned} \Delta Z_p &= \frac{Z_{p2} - Z_{p3}}{Z_{p1} - Z_{p2}} \\ \Delta Z_s &= \frac{Z_{s2} - Z_{s3}}{Z_{s1} - Z_{s2}} \end{aligned} \quad (55)$$

When  $\Delta Z$  is close to 1, the impedance gradient between the matrix and coating matches that between the coating and the fiber, weakening the scattering effect.

The shear modulus affected both the wave velocities and wave impedance. Stiffer coatings ( $\mu_2/\mu_1 = 2$ ), with  $\Delta Z_p$  close to 1, reduced dynamic stress concentrations factors (Fig. 4e and f). As  $\Delta Z_p$  approached 1, the wave impedance gradient decreased, weakening scattering, and  $\sigma_{\theta\theta}^*$  and  $\sigma_{vm}^*$  generally decreased. Although  $\Delta Z_s$  for stiffer coatings were further from 1, this effect was small compared to the effect of P wave impedance because the matrix and fiber had S wave impedances substantially lower than their P wave impedances.

As the Poisson ratio of the coating decreased with all other parameters held constant and shear modulus and density fixed as  $\mu_2 = \mu_3$  and  $\rho_2 = \rho_3$ , a modest reduction of dynamic stress concentration factors  $\sigma_{\theta\theta}^*$  and von Mises stress  $\sigma_{vm}^*$  was observed, all less than 10%, and little effect was observed on the angular locations of their maximum values (Fig. 5). This was expected from the standpoint of wave impedance: although Poisson's ratio affects compressional wave velocity, its effect on P wave impedance and the gradient  $\Delta Z_p$  is small (Fig. 5e), and it has no effect on transverse wave velocity or S wave impedance (Fig. 5f).

Substantial effects of coating density (increasing  $\rho_2/\rho_1$ ) were evident only for higher frequencies ( $\omega^* \geq 1$ ), with dynamic stress

concentrations increasing with coating density in this range when holding all other parameters constant and setting  $v_2 = v_3$  and  $\mu_2 = \mu_3$  (Fig. 6). This again was due partially to effects the wave impedance, with both  $\Delta Z_p$  and  $\Delta Z_s$  increasing with coating density, and partially due to effects of density on inertial force (Eq. (1)). The latter appears to have dominated at higher frequencies because, as seen from Eq. (1),  $F_{inertia} \propto \rho \ddot{\mathbf{u}} \propto \rho(\omega^*)^2$ . That is to say, the effect of the density on the right-hand term of Eq. (1) will be amplified by the term  $(\omega^*)^2$ . When the frequency is very low (e.g.  $\omega^* = 0.02$ ), the role of inertia is so weak ( $\rho \ddot{\mathbf{u}} \approx 0$ ) that no matter how the density is changed, both the normalized hoop stress  $\sigma_{\theta\theta}^*$  and von Mises stress  $\sigma_{vm}^*$  differ insignificantly from the quasistatic values associated with  $\rho \ddot{\mathbf{u}} = 0$  (Fig. 6). Because of this parabolic relationship, the influence of coating density was attenuated for  $\omega^* \ll 1$ , but became increasingly important as  $\omega^*$  approached 1, and dominant for  $\omega^* > 1$ .

Dynamic stress concentrations decreased with increasing coating thickness for stiff coatings with  $\mu_2/\mu_1 = 2$ ,  $\rho_2 = \rho_3$  and  $v_2 = v_3$  (Fig. 7). This was expected because, first, for stiff coatings with  $\mu_2/\mu_1 = 2$ , coatings reduce the dynamic stress concentration, and second, increasing the thickness of the coating increases the wave impedance of the inclusion (the combined coating and fiber), leading to the decrease of the wave impedance gradient. Therefore, the thickness of the coating can be tailored to effectively reduce dynamic stress concentrations in fiber reinforced composite materials.

For continuous waves, we studied the loading frequency range of  $0 < \omega^* < 2$ . Before progressing to study transient waves such as impact loading by superimposing multiple continuous waves, as will be done in the next section, we evaluated how dynamic

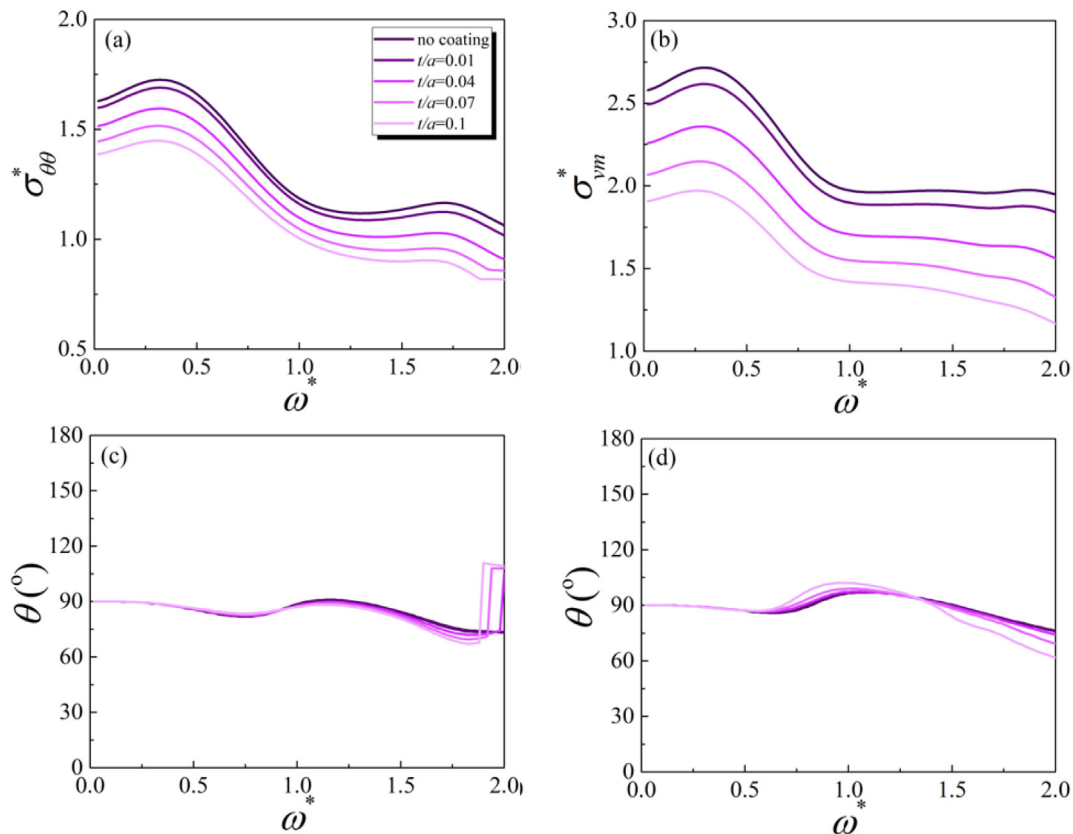
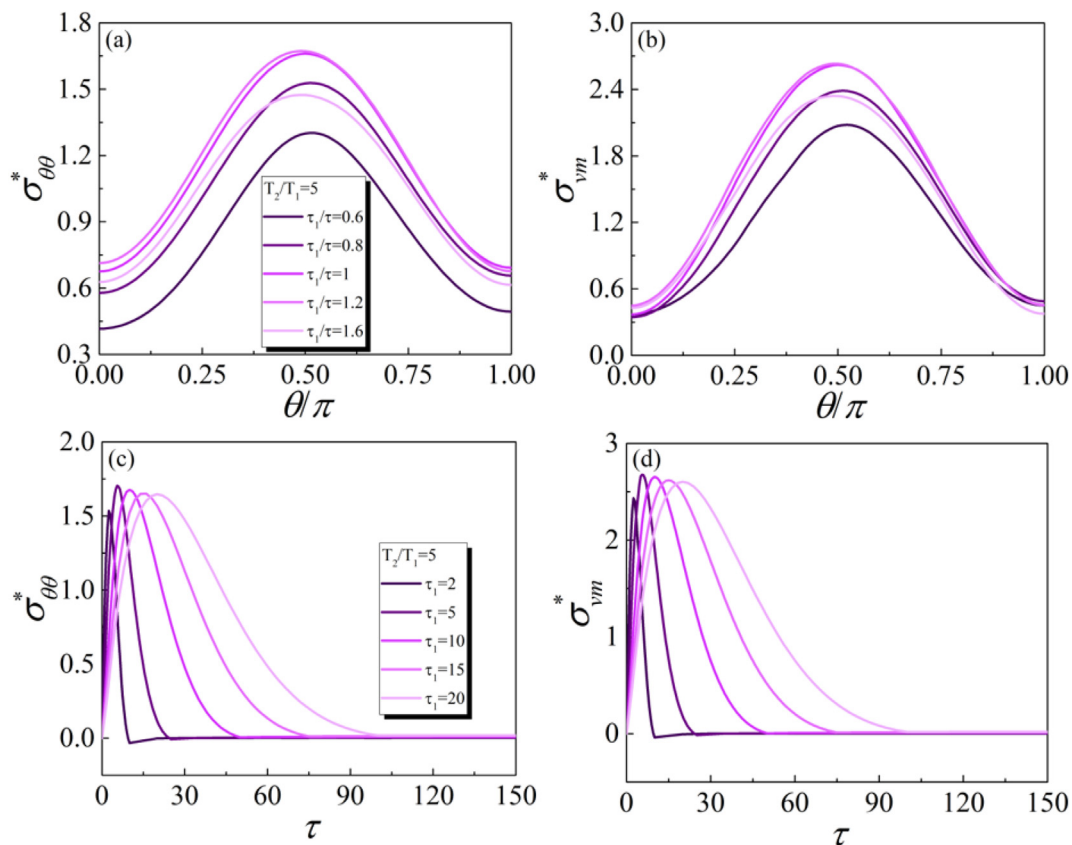


Fig. 7. (a) Normalized hoop stress  $\sigma_{\theta\theta}^*$  and (b) von Mises stress  $\sigma_{vm}^*$  plotted as the function of normalized frequency  $\omega^*$  for selected values of coating thickness  $t/a$  with  $\mu_2/\mu_1 = 2$ ,  $\rho_2 = \rho_3$ , and  $v_2 = v_3$ . (c) Angular location of maximum hoop stress for different coating thickness  $t/a$ . (d) Angular location of maximum von Mises stress for different coating thickness  $t/a$ .



**Fig. 8.** (a) Normalized hoop stress  $\sigma_{\theta\theta}^*$  and (b) von Mises stress  $\sigma_{vm}^*$  plotted as the function of position  $\theta/\pi$  for selected values of  $\tau_i/\tau$  with  $T_2/T_1 = 5$ . (a) Normalized hoop stress  $\sigma_{\theta\theta}^*$  and (b) von Mises stress  $\sigma_{vm}^*$  plotted as the function of normalized time  $\tau$  for selected values of  $\tau_i$  with  $T_2/T_1 = 5$ .

stresses from continuous waves over this relatively narrow range could be attenuated by a coating. For continuous waves, inertial effects became increasingly important at higher  $\omega^*$  ( $\omega^* > 1$ ), and were negligible for lower  $\omega^*$  (e.g.  $\omega^* = 0.01$ ). An interesting result is that the dynamic stress concentration could be attenuated across this entire range through judicious choice of the coating shear modulus.

As mentioned above, in the continuous wave problem, the inertial term on the right-hand side of the wave equation (Eq. (1)) becomes small relative to other terms for low  $\omega^*$ , and the problem approaches a static problem. The shear modulus affects both terms on the left-hand side of Eq. (1), while the Poisson ratio affects only the Lamé constant  $\lambda$  in the first. For low frequency loading, the coating shear modulus had strong effect on dynamic stress concentrations (Fig. (4)), while Poisson's ratio had little effect (Fig. (5)). As frequency increased and the problem became dynamic, the coating's affect on wave impedance reduced the dynamic stress concentration for the range ( $\mu_2/\mu_1 \leq 2$ ) studied. Thus, stiffer coatings reduced stress concentrations for the entire range studied.

Increasing the coating thickness decreased the magnitude of the impedance gradient between the matrix and fiber, and thus decreased the dynamic stress concentration (Fig. (7)). Coating density had a more complicated effect because it affected the inertial force in the governing equation (Eq. (1)). For  $\omega^* \rightarrow 0$ , the density could not raise the inertial terms to become significant compared to the left-hand side of Eq. (1) and  $\sigma_{\theta\theta}^*$  and  $\sigma_{vm}^*$  deviated insignificantly from their quasi-static values. For higher  $\omega^*$ , inertial effects became significant because the coating density effect scales as  $(\omega^*)^2$  and dominates as  $\omega^*$  nears and exceeds 1 (Fig. (6)). Thus, the effects of coating density are pronounced for very high frequencies ( $\omega^* > 1$ ), but are insignificant for lower frequencies.

### 3.3. Transient waves

For an impact loading like that of Fig. 2, the stress concentrations around a fiber with no coating were highest near the poles of the fiber ( $\theta = \pm\pi/2$ , Fig. 8a,b) for the baseline case of with  $T_2/T_1 = 5$  and normalized pressure increase time  $\tau_i = 5$ . For the baseline case, the dynamic stress concentration factors increased to a peak above 1 when the transient wave reached its peak pressure, with  $\sigma_{\theta\theta}^*$  and  $\sigma_{vm}^*$ , increasing monotonically to a maximum over a timescale close to  $\tau_i$  before decreasing monotonically back to 0 (Fig. 8c,d). This established that transient waves can cause dynamic stress concentrations and motivated us to explore whether coatings can be designed to alleviate these.

We first studied coatings in the presence of baseline transient waves ( $T_2/T_1 = 5$  and  $\tau_i = 5$ ). For a fiber coated with a material of modulus intermediate to that of the fiber and matrix and with all other properties matching those of the matrix ( $\rho_2 = \rho_3$  and  $\nu_2 = \nu_3$ ), dynamic stress concentrations decreased with increasing coating modulus (Fig. 9a,b). For these coatings and the case of  $\mu_2/\mu_1 = 2$ , dynamic stress concentrations decreased with increasing coating stiffness (Fig. 9c,d). Poisson's ratio had limited effect on dynamic stress concentrations (Fig. 9e and f). These trends all followed those of the continuous wave analyses, as was expected because the latter was used as the admittance function for the transient wave case.

However, the effect of density changed substantially, and had very little effect on the dynamic stress concentrations caused by transient wave for the case of  $\nu_2 = \nu_3$  and  $\mu_2 = \mu_3$  and changed the coating density (Fig. 9g,h). This was in stark contrast to effects of density, especially at high frequency, for a continuous wave. To explain this contradiction, we examined Eqs. (50) and (51) and

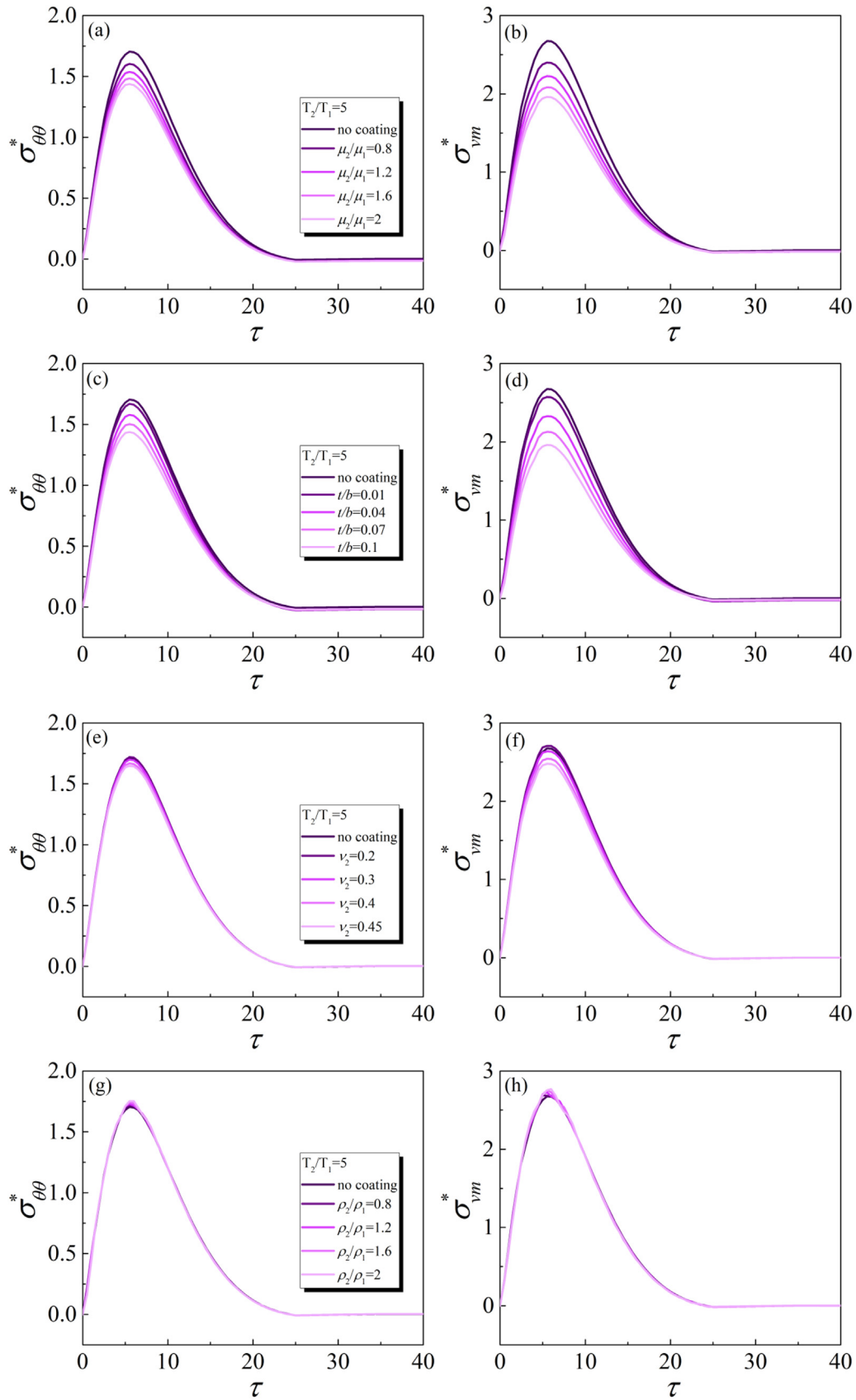


**Fig. 9.** (a) Normalized hoop stress  $\sigma_{\theta\theta}^*$  and (b) von Mises stress  $\sigma_{vm}^*$  plotted as the function of normalized time  $\tau$  for selected values of coating shear modulus  $\mu_2/\mu_1$ ; (c) Normalized hoop stress  $\sigma_{\theta\theta}^*$  and (d) von Mises stress  $\sigma_{vm}^*$  plotted as the function of normalized time  $\tau$  for selected values of coating thickness  $t/a$ ; (e) Normalized hoop stress  $\sigma_{\theta\theta}^*$  and (f) von Mises stress  $\sigma_{vm}^*$  plotted as the function of normalized time  $\tau$  for selected values of coating Poisson ratio  $\nu_2$ ; (g) Normalized hoop stress  $\sigma_{\theta\theta}^*$  and (h) von Mises stress  $\sigma_{vm}^*$  plotted as the function of normalized time  $\tau$  for selected values of coating density  $\rho_2/\rho_1$ .

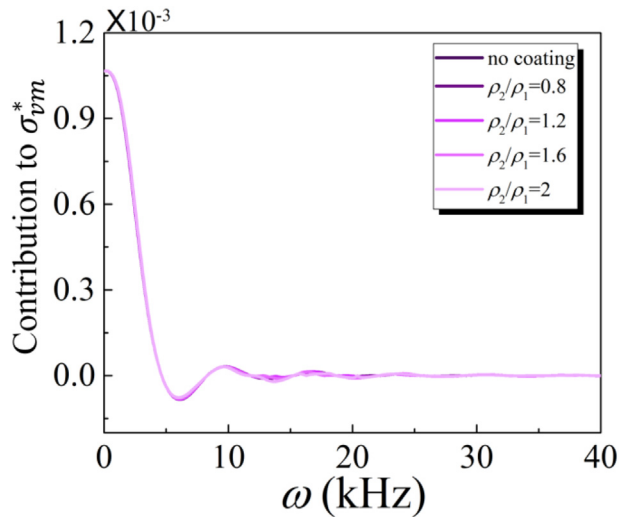


**Fig. 10.** Relative contribution of different frequencies to the dynamic part of  $\sigma_{vm}^*$ . Shown is  $g(x_i, t)$  (cf. Eqs. (50)–(51)) as a function of circular frequency  $\omega$  for selected coating densities  $\rho_2/\rho_1$ .

found that most wave energy concentrated in the low-frequency range, especially  $0 < \omega < 5\text{kHz}$  (Fig. 10), corresponding to a normalized frequency ranged of  $0 \leq \omega^* < 0.84$ . As seen from Fig. 6, the density of the coating had little effect on dynamic stresses for this low frequency range. Thus, at the lower frequencies for which the integral part contributed most to  $\sigma_{\theta\theta}^*$  and  $\sigma_{vm}^*$ , the coating density had only slight effect on dynamic response, while at the for higher frequencies for which coating density had a greater effect, the integral part contributed little to  $\sigma_{\theta\theta}^*$  and  $\sigma_{vm}^*$ , leaving little effect of coating density for these transient waves.

### 3.4. Reduction of stresses through tailored coatings

For our model composite material system and our model continuous and transient waves, dynamic stress concentrations in the matrix can be reduced in the following ways. Decreasing coating density reduces dynamic stress concentrations for the continuous wave loading case at high frequency. Increasing the stiffness and thickness of the coating reduces dynamic stress concentrations for both the continuous and transient loading cases. Poisson’s ratio has little effect. For the model composite system studied, with the constraint that the properties of the coating must lie between

those of the fiber and those of the matrix, the goal is to find a material with a stiffness as large as possible compared to that of Ti and a density as close as possible to that of carbon fibers, with a thickness as great as possible. Although technical ceramics exist in both the stiffness and density range of interest, none have both the stiffness and density range required (Ashby and Cebon, 1993). However, an example that falls within the correct range is SiC. For a loading of continuous wave, this coating can reduce the peak dynamic hoop stress  $\sigma_{\theta\theta}^*$  and dynamic von Mises stress  $\sigma_{vm}^*$  by 3.4–24% (Fig. 11a) and 6.2–40% (Fig. 11b), respectively, for coatings with thickness ranging from 0.01 to 0.1 times the radius of the carbon fiber.

## 4. Conclusions

Exact expressions for scattering from a coated fiber in an isotropic elastic medium were derived for plane compressional and transient waves. Results demonstrate that the dynamic stress concentrations at the fiber/matrix interface can be substantial compared to stress concentrations associated with static loadings at particular frequencies of the incident waves. A coating can attenuate these dynamic stress concentrations. For the cases of both continuous and transient wave loading, numerical results reveal that the shear modulus of the coating can change the wave impedance of the coating and tune the scattering effect, leading to reduction of dynamic stress concentrations. The coating’s Poisson ratio has little effect on wave impedance, and its effects on dynamic stress concentrations are thus limited. The coating density can affect the inertial force, with higher density coatings increasing dynamic stress concentrations for high frequency continuous wave loading, but not affecting transient loading in the range studied. The thickness of the coating also affects dynamic stress concentrations. Results offer guidance for designing advanced fiber reinforced composite materials.

## Declaration of Competing Interest

The authors declare that they have no known competing financial interests or personal relationships that could have appeared to influence the work reported in this paper.

## Acknowledgements

This work was supported in part by the National Natural Science Foundation of China (11972185, 11772248), the China

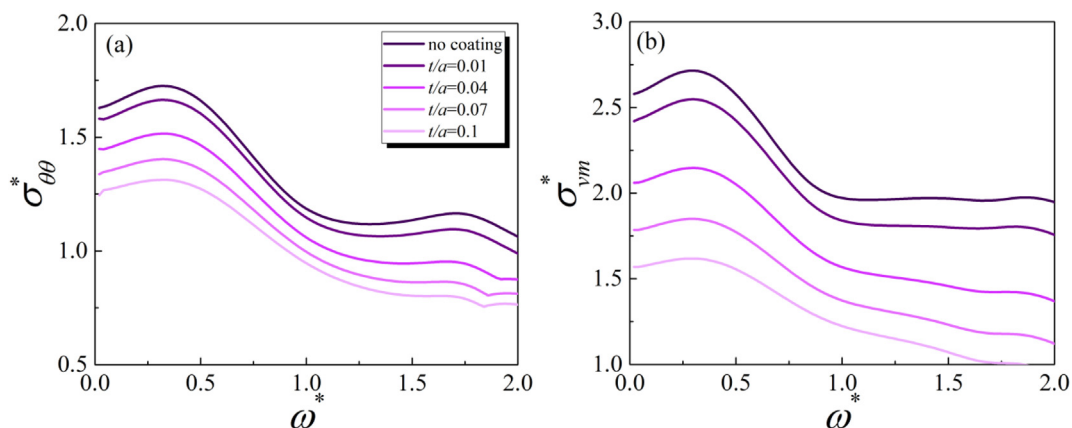


**Fig. 11.** (a) Normalized hoop stress  $\sigma_{\theta\theta}^*$  and (b) von Mises stress  $\sigma_{vm}^*$  plotted as a function of normalized frequency  $\omega^*$  for selected values of coating thickness  $t/\alpha$ , plotted for the case of a SiC coating ( $\mu_2 = 415\text{GPa}$ ,  $\rho_2 = 3205\text{kg/m}^3$ , and  $\nu_2 = 0.17$ ) (Leão-Neto et al., 2017).

Scholarship Council (201906280470), and the NIH through grant R01AR077793.

## References

- Ashby, M.F., Cebon, D., 1993. Materials selection in mechanical design. *Le J. de Physique IV 03 (C7)*, C7-1–C7-9.
- Kyriakides, S., Arseculeratne, R., Perry, E.J., Liechti, K.M., 1995. On the compressive failure of fiber reinforced composites. *Int. J. Solids Struct.* 32 (6-7), 689–738.
- Lu, T.J., 1996. Crack branching in all-oxide ceramic composites. *J. Am. Ceram. Soc.* 79 (1), 266–274.
- Evans, A.G., Zok, F.W., McMeeking, R.M., 1995. Fatigue of ceramic matrix composites. *Acta Metall. Mater.* 43 (3), 859–875.
- Genin, G.M., Hutchinson, J.W., 1999. Failures at attachment holes in brittle matrix laminates. *J. Compos. Mater.* 33 (17), 1600–1619.
- Genin, G.M., Hutchinson, J.W., 1997. Composite laminates in plane stress: constitutive modeling and stress redistribution due to matrix cracking. *J. Am. Ceram. Soc.* 80 (5), 1245–1255.
- Aveston, J., Kelly, A., 1973. Theory of multiple fracture of fibrous composites. *J. Mater. Sci.* 8 (3), 352–362.
- Budiansky, B., Hutchinson, J.W., Evans, A.G., 1986. Matrix fracture in fiber-reinforced ceramics. *J. Mech. Phys. Solids* 34 (2), 167–189.
- Rajan, V.P., Zok, F.W., 2013. Remediation of a constitutive model for ceramic composite laminates. *Compos. A Appl. Sci. Manuf.* 52, 80–88.
- Paskaramoorthy, R., Meguid, S.A., 1999. Large internal stresses in particle-reinforced composites subjected to dynamic loads. *Compos. Sci. Technol.* 59 (9), 1361–1367.
- Davidson, D.L., 1991. The effect of particulate SiC on fatigue crack growth in a cast-extruded aluminum alloy composite. *Metall. Trans. A* 22 (1), 97–112.
- Bugarin, S., Paskaramoorthy, R., Reid, R.G., 2012. Influence of the geometry and material properties on the dynamic stress field in the matrix containing a spheroidal particle reinforcement. *Compos. B* 43 (2), 272–279.
- Wang, Z., Chen, T.-K., Lloyd, D.J., 1993. Stress distribution in particulate-reinforced metal-matrix composites subjected to external load. *Metall. Trans. A* 24 (1), 197–207.
- Kassam, Z.H.A., Zhang, R.J., Wang, Z., 1995. Finite element simulation to investigate interaction between crack and particulate reinforcements in metal-matrix composites. *Mater. Sci. Eng., A* 203 (1-2), 286–299.
- Eshelby, J.D., 1957. The determination of the elastic field of an ellipsoidal inclusion, and related problems. *Proc Royal Soc London* 241 (1226), 376–396.
- Benveniste, Y., Dvorak, G.J., Chen, T., 1989. Stress fields in composites with coated inclusions. *Mech. Mater.* 7 (4), 305–317.
- Bonfoh, N., Hounkpati, V., Sabar, H., 2012. New micromechanical approach of the coated inclusion problem: Exact solution and applications. *Comput. Mater. Sci.* 62, 175–183.
- Chen, X., He, W., Liu, S., Li, M., Genin, G.M., Xu, F., Lu, T.J., 2019. Volumetric response of an ellipsoidal liquid inclusion: implications for cell mechanobiology. *Acta Mech. Sin.* 35 (2), 338–342.
- Chen, X., et al., Translation of a Coated Rigid Spherical Inclusion in an Elastic Matrix: Exact Solution, and Implications for Mechanobiology. *Journal of Applied Mechanics*, 2019. 86(5).
- Lipinski, P., Barhdadi, E.H., Cherkaoui, M., 2006. Micromechanical modelling of an arbitrary ellipsoidal multi-coated inclusion. *Phil. Mag.* 86 (10), 1305–1326.
- Sarvestani, A.S., 2003. On the overall elastic moduli of composites with spherical coated fillers. *Int. J. Solids Struct.* 40 (26), 7553–7566.
- Achenbach, J.D., Zhu, H., 1989. Effect of interfacial zone on mechanical behavior and failure of fiber-reinforced composites. *J. Mech. Phys. Solids* 37 (3), 381–393.
- Gillies, A.R., Lieber, R.L., 2011. Structure and function of the skeletal muscle extracellular matrix. *Muscle Nerve* 44 (3), 318–331.
- Mouw, J.K., Ou, G., Weaver, V.M., 2014. Extracellular matrix assembly: a multiscale deconstruction. *Nat. Rev. Mol. Cell Biol.* 15 (12), 771–785.
- Podratz, J.L., Rodriguez, E., Windebank, A.J., 2001. Role of the extracellular matrix in myelination of peripheral nerve. *Glia* 35 (1), 35–40.
- Choi, J.B., Youn, I., Cao, L.I., Leddy, H.A., Gilchrist, C.L., Setton, L.A., Guilak, F., 2007. Zonal changes in the three-dimensional morphology of the chondron under compression: the relationship among cellular, pericellular, and extracellular deformation in articular cartilage. *J. Biomech.* 40 (12), 2596–2603.
- Saadat, F. et al., 2018. Functional grading of pericellular matrix surrounding chondrocytes: potential roles in signaling and fluid transport. *bioRxiv* 365569.
- Madhukar, M.S., Drzal, L.T., 1991. Fiber-matrix adhesion and its effect on composite mechanical properties. I. Inplane and interlaminar shear behavior of graphite/epoxy composites. *J. Compos. Mater.* 25 (8), 932–957.
- Walpole, L.J., 1978. A coated inclusion in an elastic medium. *Math. Proc. Cambridge Philos. Soc.* 83 (3), 495–506.
- Mikata, Y., Taya, M., 1985. Stress field in a coated continuous fiber composite subjected to thermo-mechanical loadings. *J. Compos. Mater.* 19 (6), 554–578.
- Chen, X., Li, M., Yang, M., Liu, S., Genin, G.M., Xu, F., Lu, T.J., 2018. The elastic fields of a compressible liquid inclusion. *Extreme Mech. Lett.* 22, 122–130.
- Ghosh, L.J., Lerch, B.A., 1989. Optimum interface properties for metal matrix composites. *Compos. Mater.*
- Evans, A., Zok, F., Davis, J., 1991. The role of interfaces in fiber-reinforced brittle matrix composites. *Compos. Sci. Technol.* 42 (1-3), 3–24.
- Zhang, J., Fan, J., Zhang, J., Zhou, J., Liu, X., Qie, D., Zhang, D., 2018. Developing and preparing interfacial coatings for high tensile strength silicon nitride fiber reinforced silica matrix composites. *Ceram. Int.* 44 (5), 5297–5303.
- Carman, G.P., Averill, R.C., Reifsnider, K.L., Reddy, J.N., 1993. Optimization of fiber coatings to minimize stress concentrations in composite materials. *J. Compos. Mater.* 27 (6), 589–612.
- Frueh, S.J., Coons, T.P., Reutenauer, J.W., Gottlieb, R., Kmetz, M.A., Suib, S.L., 2018. Carbon fiber reinforced ceramic matrix composites with an oxidation resistant boron nitride interface coating. *Ceram. Int.* 44 (13), 15310–15316.
- Bogan, S.D., Hinders, M.K., 1993. Dynamic stress concentrations in fiber-reinforced composites with interface layers. *J. Compos. Mater.* 27 (13), 1272–1311.
- Wang, Z.-L., Li, Y.-C., Shen, R.F., 2007. Numerical simulation of tensile damage and blast crater in brittle rock due to underground explosion. *Int. J. Rock Mech. Min. Sci.* 44 (5), 730–738.
- Pamel, A.V. et al., 2017. Finite-element modelling of elastic wave propagation and scattering within heterogeneous media. *Proc. Royal Soc. A: Math. Phys. Eng. Sci.* 473 (2197), 20160738.
- Xu, C. and Z. Yu, Numerical simulation of elastic wave propagation in functionally graded cylinders using time-domain spectral finite element method. *Advances in Mechanical Engineering*, 2017. 9(11): p. 1687814017734457.
- Pao, Y.-H., C.-C. Mow, Diffraction of elastic waves and dynamic stress concentrations. New York: Crane, Russak & Co., 1973.
- Pao, Y.H., Mow, C.C., 1976. Theory of normal modes and ultrasonic spectral analysis of the scattering of waves in solids. *J. Acoust. Soc. Am.* 59 (5), 1046–1056.
- Pao, Y.-H., 1962. Dynamical stress concentration in an elastic plate. *J. Appl. Mech.* 29 (2), 299–305.
- Wang, Q., Cao, F., Xiang, Y., Peng, Z.-H., 2017. Effects of ZrO<sub>2</sub> coating on the strength improvement of 2.5 D SiCf/SiO<sub>2</sub> composites. *Ceram. Int.* 43 (1), 884–889.
- He, H., Duan, Z., Liang, W., Wang, Z., Luo, N.a., 2019. Improving comprehensive mechanical properties of glass fiber reinforced composites by coating the ternary multiscale modifier. *Mater. Res. Express* 6 (12), 125309. <https://doi.org/10.1088/2053-1591/ab5565>.
- Verbis, J., Tsinopoulos, S., Polyzos, D., 2002. Elastic wave propagation in fiber reinforced composite materials with non-uniform distribution of fibers. *Comput. Model. Eng. Sci.* 3 (6), 803–814.
- Leão-Neto, J.P., Lopes, J.H., Silva, G.T., 2017. Scattering of a longitudinal Bessel beam by a sphere embedded in an isotropic elastic solid. *J. Acoust. Soc. Am.* 142 (5), 2881–2889.
- Mahmoudian, F., Margrave, G.F., 2007. P-wave impedance. Application to VSP data from Alberta. in CSPG CSEG convention, S-wave impedance and density from linear AVO inversion.
- Peng, X., He, W., Xin, F., Genin, G.M., Lu, T.J., 2020. The acoustic radiation force of a focused ultrasound beam on a suspended eukaryotic cell. *Ultrasonics* 108, 106205. <https://doi.org/10.1016/j.ultras.2020.106205>.
- Peng, X. et al., 2020. Standing surface acoustic waves, and the mechanics of acoustic tweezer manipulation of eukaryotic cells. *J. Mech. Phys. Solids* 145, 104134.